Comparative Study of the Thermoresistive Behavior of Carbon Nanotube-Based Nanocomposites and Multiscale Hybrid Composites

Hongbo Dai[1], Erik T. Thostenson[1,2,3*] and Thomas Schumacher[4]

[1] Center for Composite Materials, University of Delaware, Newark, Delaware 19716, United States
[2] Department of Mechanical Engineering, University of Delaware, Newark, Delaware 19716, United States
[3] Department of Materials Science and Engineering, University of Delaware, Newark, Delaware 19716, United States
[4] Department of Civil and Environmental Engineering, Portland State University, Portland, Oregon, 97201, United States

ABSTRACT

Advances in carbon nanotube (CNT) based composites over the past decade have demonstrated broad potential of utilizing them as multifunctional sensors because of their unique electrical properties. This article studies the thermoresistive behavior of binary-phase (CNT-epoxy) nanocomposites and ternary-phase hierarchical (CNT-fiber-epoxy) multiscale composites using *in situ* electrical resistance measurements during thermal cycling from 25-145ºC. A series of CNT-based composites with controlled nanotube morphologies were created via three-roll-milling, dip-coating and electrophoretic deposition methods. The results show that the thermoresistive behavior of CNT-based composites is influenced by the CNT concentration, thermal expansion, fiber/polymer properties, and interfacial interactions. CNT-epoxy nanocomposites with randomly dispersed CNTs show a positive temperature correlation of resistance (TCR). In comparison, multiscale composites with fibers show a double-crossover-shaped temperature dependence of their electrical resistance that is influenced by the changes of the CNT network that are induced by the polymer thermal motions and the residual thermal stresses. The thermal expansion behavior of the composites was characterized and a finite element model was used to examine the fiber-matrix interfacial residual stresses. While the thermoresistive behavior of nanocomposites has been investigated more broadly, this research is a first step in understanding the processing-structure-thermoresistive response relationship of multiscale CNT/fiber composites.

Key Words: Carbon nanotube (CNT), nanocomposite, multiscale composite, thermoresistive behavior, temperature correlation of resistance (TCR)

* Corresponding author.
Tel: 302 831-8789.
E-mail address: thosten@udel.edu (Erik T. Thostenson)

1. Introduction

The remarkable mechanical, electrical and thermal properties of carbon nanotubes (CNTs) has stimulated broad interest in the development of CNT-based nanocomposites [1,2,3]. While their reported high specific stiffness and strength motivated their use as nanoscale structural reinforcements [4,5], recent attention has focused on utilizing CNTs as a multifunctional additive for sensing applications. For example, CNT-based composites have been used as piezoresistive sensors for strain and damage detection [6-9] and structural health monitoring [10]. Other sensing applications examined for CNT-based composites include the detection of external stimuli including pressure [11,12], vapor [13,14], temperature [15,16], humidity [17], infrared radiation [18,19], and chemicals [14,20]. For practical applications, these sensors are exposed to varying temperatures throughout their use, and the temperature dependence of the electrical resistance, known as the thermoresistive behavior, must be considered when examining the response of CNT-based sensors.

Individual CNTs can have varying morphologies ranging from the tube-level, such as single-walled carbon nanotubes (SWCNT) or mutli-walled carbon nanotubes (MWCNT), to hierarchical structures including entangled CNT networks, ropes, bundles, mats, and films. In addition to CNT-based nanocomposites, where CNTs are dispersed within a polymer matrix, there is increasing interest in combining reinforcement scales of nanoscale reinforcements with traditional micron-sized structural reinforcements. These composites often referred to as multiscale hybrid or hierarchical composites are distinctly different in terms of the morphology of nanotube networks as well as the interactions between the structural reinforcement and the CNTs. These various CNT-based composites may demonstrate distinctive thermoresistive behavior due to a broad range of physical and chemical interactions. Individual SWCNT can be either metallic or semiconducting. Metallic SWCNTs show an increase in electrical resistance with increasing temperature raises, known as a positive temperature correlation (PTC). For semiconducting SWCNTs, the resistance decreases with increased temperatures and show a negative temperature correlation (NTC) depending on the tube diameter and chirality [21-23]. For MWCNTs only the outermost layer contributes to its electrical conduction [24,25]. Large diameter MWCNTs mostly show a metallic character with weak inter-tube coupling [26] while small-diameter MWCNTs behave similarly to SWCNTs [27].

Fischer *et al*. [28,29], Hone *et al*. [30], Bae *et al*. [31] and Skakalova *et al*. [26] have studied the electrical transport phenomena in SWCNT-thin films and thick mats. They found that both macroscopic networks of SWCNTs are semiconducting at low temperatures but are metallic above room temperature, following the interrupted metallic conduction model [32]. This response is dominated by the Schottky contacts between metallic and semiconducting tubes for the thin-network of SWCNTs [26,33] and by the metallic tube-tube junctions for the thick-network of SWCNTs [26,31,34]. In comparison, MWCNT films show semiconducting behavior over a wide range of investigated temperatures, such as -272 to 27ºC [35,36], -150 to 300ºC [37], -48 to 147ºC [15], 20 to 150ºC [38], and 27 to 1627ºC [39]. The conduction mechanisms in these films are dominated by defects in tubes and inter-tube contacts at low temperatures and the inter-tube tunneling dominates at higher temperatures [36].

Electrical conduction mechanisms become further complicated when CNTs are dispersed into polymers and the experimental data are widely scattered in literature. For example, Barrau *et al*. [40] studied the DC conductivity of the MWCNT-epoxy composites with 0.4 to 2.5 wt% CNTs across a temperature range of 20-110ºC. These composites showed an NTC that is dominated by the tunneling effect in the CNT network. On the other hand, Alamusi *et al*. [41] reported a PTC of MWCNT-epoxy composites with CNT concentrations ranging from 1-5 wt% over a temperature range of 60 to 100ºC, which was attributed to the temperature-dependent CNT-CNT tunneling effect. They found that the temperature coefficient of resistance (TCR) increases with increasing temperature and MWCNT content. Cen-Puc and co-workers [42] demonstrated a PTC for MWCNT-polysulfone composites from 25 to 100ºC with CNT concentrations ranging from 0.5-25 wt%, but found the positive TCR increases as CNT content decreases. A PTC-to-NTC crossover behavior was observed in MWCNT-epoxy composites from -20 to 110ºC for concentrations of 2-3 wt% and were reported by Njuguna *et al*. [43]. In their work they showed that resistance first rises to a local peak of approximately 50ºC and then suddenly drops to a local minimum near 80ºC followed by a second increase. Based on differential scanning calorimetry and Raman spectroscopy analyses, they attributed this phenomenon to physical aging of the epoxy matrix and the rearrangement of the CNT network. MWCNT-HDPE (high-density polyethylene) composites show both PTC [44] and PTC-to-NTC crossover responses [45, 46] dominated by the CNT network and the polymer properties. NTC-to-PTC crossover behavior was also found in the thermoresistive response of 1 wt% MWCNT-polysulfone composites from -110 to 25ºC [47].

These different behaviors have been noted in a variety of different matrix materials. For example, NTC responses were observed for SWCNT-polycarbonate [18] and MWCNT-PEEK [48], MWCNT-SEBS (styrene-ethylene-butylene-styrene) [16], MWCNT-polyamide-6 [49], and MWCNT-polyurethane [50]. On the other hand, MWCNT-polypropylene [51] shows PTC, and MWCNT-vinyl ester [52] and MWCNT-PVDF (polyvinylidene fluoride) [53] demonstrate a PTC-to-NTC thermoresistive crossover response. Finally, the thin films of the SWCNT/PDDA+PSS [54] and MWCNT/PSS+PVA [55] exhibit a NTC-to-PTC crossover similar to SWCNT mats [26].

To date, there have been few investigations on the thermoresistive behavior of CNT-based multiscale, hierarchical composites. Only very few studies have been performed on small-scale composite specimens. Gao *et al*. [56] grafted MWCNTs onto a single glass fiber through a dip-coating procedure and then embedded them into an epoxy matrix, and then studied the resistive response from -150 to 180ºC, which exhibited a monotonic NTC. Later, Zhang and co-workers [57] repeated the same experiment with CNTs coated on fibers using an electrophoretic deposition (EPD) approach and found a strong PTC-NTC crossover phenomenon, which was closely correlated with local changes of polymer properties. However, a macro-level study of thermoresistive behavior of multiscale composites has not been reported in the literature.

Lessons learned from the existing literature highlighted above underlines the need to better understand the mechanisms that contribute to the thermoresistive behavior of CNT-based multiscale composites. This research investigates several key parameters that could contribute to the bulk thermoresistive response including the morphological structures of nanotubes and tube-based networks, the interfacial interactions between CNTs and the surrounding polymer, processing-induced residual stresses in the composites, and the polymer thermomechanical properties. To address these key parameters, four types of composites, illustrated in Fig. 1, with distinctive morphologies are investigated including (1) nanocomposite with randomly dispersed CNTs in epoxy, and multiscale CNT/fiber hybrid composites with (2) randomly dispersed CNTs in the matrix, (3) loosely-concentrated and (4) densely-concentrated CNTs near the fiber surface. In this work, the structure and morphology of these composites were characterized and a comparative study conducted examining the influence of morphology on their bulk thermoresistive response. A thermomechanical analyzer was used to examine the bulk thermal expansion of the composites and finite element analysis was performed to investigate the residual thermal stresses developed in fiber/epoxy composites. This investigation is aimed at creating a comprehensive

understanding of the thermoresistive behavior of CNT-based multiscale composites that is beneficial to guide their potential practical applications as sensors.

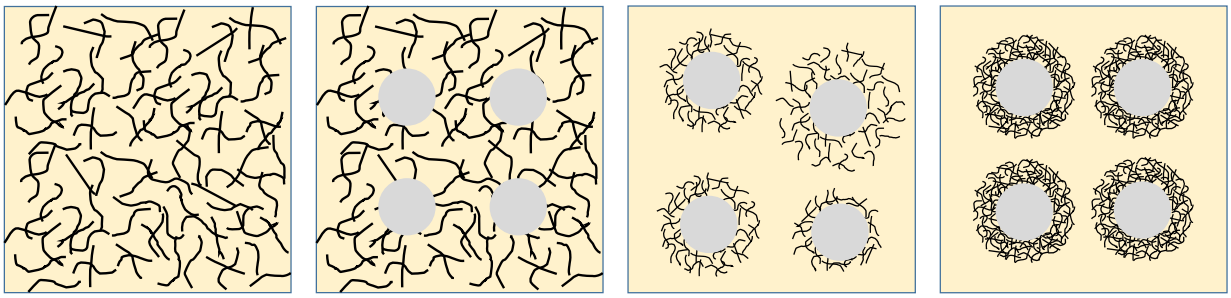

Figure. 1. Schematic illustrations of the four morphological states of the CNT-based composites evaluated in this study: (a) randomly dispersed CNTs in epoxy, (b) randomly dispersed CNTs in the matrix surrounding the fibers, (c) loosely-concentrated CNTs at the fiber-matrix interface and (d) densely concentrated CNTs in a thin coating around the fiber.

2. Experimental Methods and Simulations

2.1 Materials, Composites Manufacturing and Specimen Preparation

This section details the specific materials and manufacturing processes used to create the different morphologies highlighted in Fig. 1. For all composites the polymer matrix is an epoxy resin system composed of a bisphenol-f epichlorohydrin epoxy cured with an aromatic diamine curing agent (EPON 862 with EPIKURE W, Momentive Specialty Chemicals Inc.) at a weight ratio of 100:26.4 (862:W). All composites also underwent the same cure cycle of 130ºC for 6 hours. Prior to testing, all specimens were annealed at 130ºC and cooled in a desiccator cabinet for 48 hours in order to minimize thermal history and moisture effects. Table 1 highlights the types of specimens, processing methods, composition, and specimen geometries used in this study.

Table 1: Specimen information for different groups of CNT-based composites.

Sample Group	Processing Methods	MWCNT (wt%)	Fiber Type	Sample Dimensions (mm)	Number of Tested Samples
Nanocomposite with Randomly Dispersed CNTs	3-Roll-Milling	0.25, 0.5	None	5×15×3	12
Multiscale Composite with Loosely Concentrated CNTs	Dip-Coating & VARTM	0.05, 0.17, 0.61, 0.77, 1.0	Aramid, E-glass	13×102×0.5	36
Multiscale Composite with Densely Concentrated CNTs	EPD & VARTM	1.8, 3.4	Aramid	13×102×0.5	12

Multiscale Composite with Randomly Dispersed CNTs	3-Roll-Milling & VARTM	0.25, 0.5	Aramid, E-glass	13×102×0.5	24
Plain Nonwoven Composite (Control Sample)	VARTM	None	Aramid, E-glass	5×15×0.4	12
CNT Sizing Film on Glass Slide (Control Sample)	Dip-Coating	~ 25.0	None	15×40×0.1	6

[1] All dimensions are average values and presented as width × length × thickness.

2.1.1 Nanocomposites and CNT/Fiber Composites with Dispersed Carbon Nanotubes

In order to create CNT nanocomposites with a high degree of dispersion and a CNT/fiber composite with carbon nanotubes uniformly dispersed throughout the polymer matrix (Fig. 1a and 1b, respectively) a three-roll-mill (EXAKT 80E, EXAKT Technologies, Inc.) was used to disperse multi-walled CNTs into the epoxy resin following the technique developed in our prior research [58]. The as-received multi-walled CNTs (CM-95, 95 wt% purity, Hanwha Nanotech, Korea) are highly entangled and have diameters between 10 and 20 nm. The CNTs were weighed and mixed with the EPON 862 epoxy resin to achieve final target weight fractions of 0.25 and 0.5%. The mixture was repeatedly passed through the three-roll-mill where the adjacent rollers at gradually smaller gap settings down to the minimum setting of 5 μm. After milling, the mixture was degassed under vacuum for 20 min and the curing agent was added to the dispersion and mixed using a planetary centrifugal mixer (THINKY ARM-310). To create nanocomposites for characterization the mixture was poured into aluminum molds and cured. For CNT/fiber composites where the CNTs are uniformly dispersed in the matrix a standard vacuum assisted resin transfer molding (VARTM) approach was used [6]. CNT-epoxy resin was infused into randomly oriented aramid (Optiveil®, 27 g/m^2, with the cross-linked polyester binder) and E-glass (Optimat®, 50 g/m^2, with a polyvinyl alcohol (PVA) binder) fabrics. Technical Fiber Products, Inc. manufactured both fabrics. The fabrics, which are often used as a veil material for composites, have discontinuous fibers with a fiber length of 12 mm, binder content of 12.5 wt%, and similar porosity of about 90%.

2.1.2 Composites with Loosely-Concentrated CNTs on the Fiber Surfaces

To create composites with loosely-concentrated CNTs on the fiber surfaces (Fig. 1c) a dip-coating approach developed in our previous work [6,9,11,59] was used to deposit CNTs onto the nonwoven fabrics. A commercially-available aqueous CNT sizing dispersion (SIZICYL™ XC R2G, Nanocyl, Belgium) used in the dip-coating process and has an approximate composition of 1.5 wt% CNTs, 3.0 wt% sodium dodecyl benzene sulfonate (SDBS) surfactant, 1.5 wt% film

former, and 94% water, resulting in about 6 wt% residual solids after drying. In order to obtain composites with varying CNT concentrations, the CNT dispersion was diluted with ultra-pure water at different mass ratios (sizing:water) of 1:1, 1:2, 1:5, 1:20, and 1:50. The diluted sizing was pre-mixed using a centrifugal mixer (THINKY ARM-310) at 2000 rpm for 120 s followed by sonication for 15 min in an ultrasonic bath (Branson 1510). The fabric was then trimmed to the desired size and placed into the CNT sizing dispersion for 20 min. After drying at 160ºC, the epoxy resin was infused into the CNT-modified fabric using the VARTM process followed by curing. Five groups of aramid-sizing/epoxy composites with final concentrations of 1.0, 0.77, 0.61, 0.17, and 0.05 wt% CNTs were fabricated. An E-glass-sizing/epoxy composite with 1.0 wt% CNTs was also made for comparison.

2.1.3 Composites with Densely Concentrated CNTs on the fiber Surfaces

For creating composites with a dense and uniform CNT coating (Fig. 1d), an electrophoretic deposition (EPD) approach was employed. First, the multi-walled CNTs (CM-95, Hanwha Nanotech) were oxidized using an ultrasonicated-ozonolysis (USO) method [60,61] by bubbling ozone gas into a mixture of nanotubes and ultra-pure water under continuous sonication using a wand sonicator equipped with a flow cell (Sonicator 3000, Misonix, USA) for 15 hours. The oxidized CNTs were then functionalized with polyethylenimine (PEI, M_w = 25,000, Sigma-Aldrich) and sonicated for another two hours. The pH of the dispersion was adjusted to 6.0 using glacial-acetic acid (Sigma-Aldrich, USA) [60] in order to protonate the PEI and to have a zeta potential of the positively-charged CNTs of about +40 mV. Next, EPD of the PEI-functionalized CNTs onto a sheet of aramid nonwoven fabric was performed at room temperature using stainless steel electrodes [60,61]. The fabric was placed firmly on the cathode and fully immersed in the CNT (1.0 g/L) dispersion. Cathodic depositions were conducted under a constant DC field of 37.5 V/cm with deposition times of 5 and 10 min. After drying the fabric at room temperature for 24 hours, the epoxy resin was infused into the CNT-coated fabric via VARTM. Two groups of aramid-EPD CNT/epoxy composites with 1.8 and 3.4 wt% CNTs were finally produced.

2.1.3 Reference Specimens for Thermomechanical and Thermoresistive Measurements

For thermomechanical characterization, a set of reference specimens of the nonwoven aramid and E-glass fabric were manufactured without any CNTs using the same VARTM approach. The composites without CNTs are electrically insulating. For thermoresistive characterization, an

additional set of specimens were created by depositing films onto glass slides by dip-coating the CNT dispersion.

2.2 Materials Characterization and Simulation

2.2.1 Scanning Electron Microscopy

Scanning electron microscopy (AURIGA™ 60 Crossbeam™ FIB-SEM with 3~5kV accelerating voltages) was used to examine the morphologies of the different composite systems used in this study. To view the hierarchical morphology of the composites, fracture surfaces of the different CNT-based composites were imaged. The composite specimens were fractured after freezing in liquid nitrogen for 5 min. To minimize sample charging, all fracture surfaces were coated with a thin conductive Pt/Au layer (~5 nm) in a vacuum sputter coater (Denton Desk IV, Denton Vacuum, LLC) prior to imaging.

2.2.2 Thermomechanical Analysis

The composite thermomechanical behavior was studied using a thermomechanical analyzer (TMA; Hyperion® TMA 402 F1, Netzsch). The samples were heated to 180ºC from room temperature at a ramp rate of 2ºC/min in a nitrogen environment at a flow rate of 20 mL/min. Neat epoxy and CNT nanocomposite specimens were tested under expansion mode using a flat probe, while the thin composite layers were tested using a tensile clamp with a 10 mm gage length. A static force of 100 mN was applied by the TMA probe to all specimens while testing. The linear coefficient of thermal expansion (CTE) is calculated based on the normalized change of specimen length with temperature.

2.2.3 In situ Thermoresistive Characterization

For thermoresistive characterization, electrodes were created by applying silver paint (SPI Supplies®, Structure Probe, Inc.) to the ends of the specimens and anchoring wires with a silver filled conductive epoxy (EPOXIES®40-3900, Epoxies, Etc.) and cured at 90ºC for 30 minutes. The specimens were tested in an environmental chamber (CSZ Z8-plus, Cincinnati Sub-Zero) and subjected to a total of three temperature cycles between 25 and 145ºC at a ramp rate of 2ºC/minute. An isothermal segment was programmed at 25 and 145ºC to ensure the specimens reach thermal equilibrium. The electrical properties of the CNT-based composites as well as temperature were measured in real-time using a data acquisition system controlled by a customized LabVIEW program (National Instruments). This integrated system contains Keithley 3706A System

Switch/Multimeter, Keithley 3750-ST terminal block, NI-SC-2345 signal conditioner, NI-SCC-TC02 module, and a Type-K thermocouple. The specimens were tested under a constant current, which was varied between 10 mA to 10 μA depending on the volume resistivity of the tested specimen. Resistance was calculated based on measured voltage change. Results are presented as normalized percentage in resistance change, $\Delta R/R_0$, as follows:

$$\Delta R/R_0 = (R-R_0)/R_0 \quad (1)$$

where ΔR is the resistance change, R_0 is the initial electrical resistance of the specimen at room temperature (T_0), and R is the measured transient resistance at the measured temperature (T). In addition, the temperature coefficient of resistance (TCR) is defined as the normalized resistance change with respect to the unit change of temperature and calculated as follows:

$$TCR = \frac{R-R_0}{R_0} / (T-T_0) \quad (2)$$

Volume resistivity, ρ_v, is calculated from the measured electrical resistance and the specimen dimensions:

$$\rho_v = R_0 \frac{A}{L} \quad (3)$$

where A is sample cross-sectional area and L is sample length. Table 2 summarizes the measured resistances and volume resistivity for the different specimens used in this study.

Table 2: Measured electrical resistances and volume resistivity of CNT-based composite specimens at 25 ºC.

Composite Group	R_0[1] (kΩ)	ρ_v[1] (Ω·m)
3-Roll-Mill CNT (0.5 wt%)-Epoxy	34.3±3.7	33.4±3.5
3-Roll-Mill CNT (0.25 wt%)-Epoxy	112.5±23.4	105.2±21.4
Aramid/3-Roll-Mill CNT(0.5 wt%)-Epoxy	607.4±83.6	38.0±5.2
Aramid/3-Roll-Mill CNT(0.25 wt%)-Epoxy	2811.0±644	175.7±40.3
E-Glass/3-Roll-Mill CNT(0.5 wt%)-Epoxy	1099.3±283.7	68.7±17.7
E-Glass/3-Roll-Mill CNT(0.25 wt%)-Epoxy	5792.5±1348	362.0±84.3
Aramid-Sizing (1.0 wt%CNT)/Epoxy	3.1±0.1	0.19±0.01
Aramid-Sizing (1.0 wt%CNT)/Epoxy (After Post-Cure)	2.9±0.04	0.18±0.004
Aramid-Sizing (0.77 wt%CNT)/Epoxy	4.7±0.5	0.30±0.03
Aramid-Sizing (0.61 wt%CNT)/Epoxy	7.3±0.7	0.45±0.04

Aramid-Sizing (0.17 wt%CNT)/Epoxy	66.1±3.5	3.8±0.22
Aramid-Sizing (0.05 wt%CNT)/Epoxy	402.3±28	25.0±1.7
E-Glass-Sizing (1.0 wt%CNT)/Epoxy	2.6±0.3	0.16±0.02
Aramid-EPD CNT (3.4 wt%)/Epoxy	442.4±83.4	27.2±5.1
Aramid-EPD CNT (1.8 wt%)/Epoxy	3125±534	226.8±38.8
CNT Sizing Film on Glass Slide (Control Sample)	$(60.7\pm4) \times 10^{-3}$	$(2.2\pm0.15) \times 10^{-3}$

[1]All data are shown as average value ± ½ difference between the highest and lowest value.

2.2.4 Finite Element Analysis

In fiber composites, thermal stresses result from the mismatch in CTE and Young's moduli of the fibers and the matrix [62-68]. Because CNT coatings are located near the fiber-matrix interface, thermal residual stresses may play a significant role in the thermoresistive response. To examine the stresses at the fiber-matrix interface a simplified thermal stress simulation of the local constituents including fiber and matrix was performed using COMSOL Multiphysics® (Version 4.3b) finite element (FE) analysis software. Figure 2 shows a representative volume element (RVE) of a fiber and surrounding matrix. The thermal expansion mismatch can induce stresses at the interface in the radial (σ_{rr}), hoop ($\sigma_{\theta\theta}$) and axial (σ_{zz}) directions. The three-dimensional solid model comprising a quarter of two concentric cylinders with a height of 10-μm was modeled in cylindrical coordinates

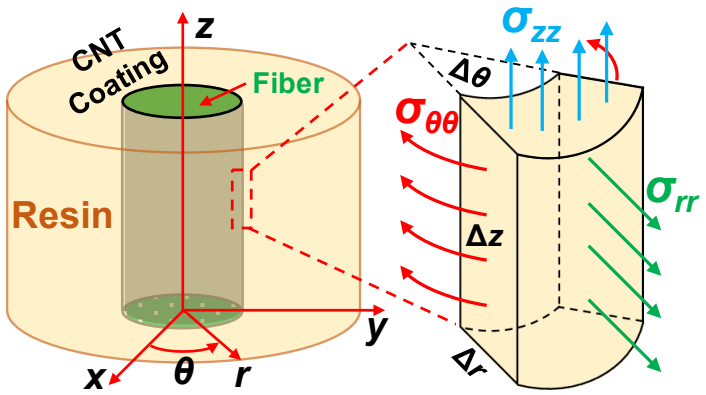

Figure 2. Schematic model of a cylindrical representative volume element from examining residual stresses at the fiber-matrix interface, and the detailed illustration showing the resolved normal stresses exerted on a typical volume element of the epoxy resin infiltrated CNT-coating on fiber surface.

The FE model has two domains with different material properties, the fiber and epoxy matrix, that are discretized using tetrahedral elements and with eight layers of finer boundary layer meshes

in between the two domains (see supplementary information, Fig. S1). The boundaries are traction-free and assigned to be symmetric. The software enforces the continuity of dependent variables across the internal boundaries between the two domains automatically. A specific temperature boundary condition was designated at the exterior surface of the matrix in the model. The initial and final temperature was set as 120ºC, near the glass transition temperature of epoxy, and 25 ºC, respectively. Above the glass transition temperature the system is assumed to be in a stress-free state [66-68] and then the thermal residual stresses are simulated during cooling. In this FE model, the E-glass fiber and epoxy are modeled as the isotropic linear elastic materials and the aramid fiber is considered as the orthotropic, transversely isotropic, linear elastic material. In real composites, carbon nanotubes are concentrated on the fiber surfaces and entirely immersed in epoxy. This fiber-CNT-resin interphase region was not directly modeled due to the lack of available effective material properties. In addition, perfect interfacial bonding was assumed between fiber and epoxy matrix. A 10 μm region surrounding the fiber and the resulting thermal stresses due to temperature changes were examined to understand the state of stress near the fiber surface. The material properties for the FE simulations are presented in Table 3.

Table 3: Material property input for the FE models.

Material	**Radius (μm)**	**Young's Modulus (GPa)**	**Poisson's Ratio**	**CTE (α) 10^{-6}/ºC**	**Thermal Conductivity (W/(m*K)**	**Heat Capacity J/(kg*K)**	**Density Kg/m^3**
Epoxy Resin (*isotropic*)	10 μm thick	2.58	0.35	72	0.202	1060	1110
E-Glass (*isotropic*)	10	75.0	0.22	5	1.275	802	2575
Aramid Fiber (*orthotropic*)	6	E_{rr} = 2.3 $E_{\theta\theta}$ = 2.3 E_{zz} = 80.0	$\nu_{r\theta}$ = 0.25 $\nu_{r\theta}$ = 0.60	α_{rr} = 78 $\alpha_{\theta\theta}$ = 78 α_{zz} = -5.4	0.040	1420	1440

3. Results and Discussion

3.1 Composite Microstructure Characterization

3.1.1 Composites with Dispersed CNTs

Figure 3a shows the fracture surface of the CNT-epoxy nanocomposite with a concentration of 0.5 wt% CNTs. The fracture surface shows significant surface roughness with numerous randomly distributed, short and curved structural features suggesting that the fracture was accompanied with localized plastic deformation [58,69]. The higher magnification image in Fig. 3b shows CNTs on

the fracture surface that are relatively short and show minimal nanotube pullout, suggesting a relatively strong interaction between CNTs and the epoxy matrix. The fracture surface of the neat epoxy (see supplementary information Figs. S2a and S2b) does not show similar microscale features and is indicative of brittle fracture. In addition, the nanocomposite with 0.25 wt% CNTs (supplementary information, Figs. S2c and 2d) shows relatively reduced surface roughness with fewer and more scattered CNTs. Figure 3c shows the fracture surface of the multiscale composites with aramid fibers and 0.5 wt% CNTs dispersed in epoxy matrix. Pullout of the aramid fibers are observed, suggesting the weak interfacial bonding between the matrix and fiber. Compared with the nanocomposite, the micron-scale surface roughness of the matrix phase is reduced. Figure 3d, shows a high magnification of the matrix fracture surface where carbon nanotubes are visible on the fracture surface. The comparatively flat fracture surface as compared to the nanocomposite suggests that most of the fracture energy was dissipated through fiber debonding and pullout rather than matrix fracture.

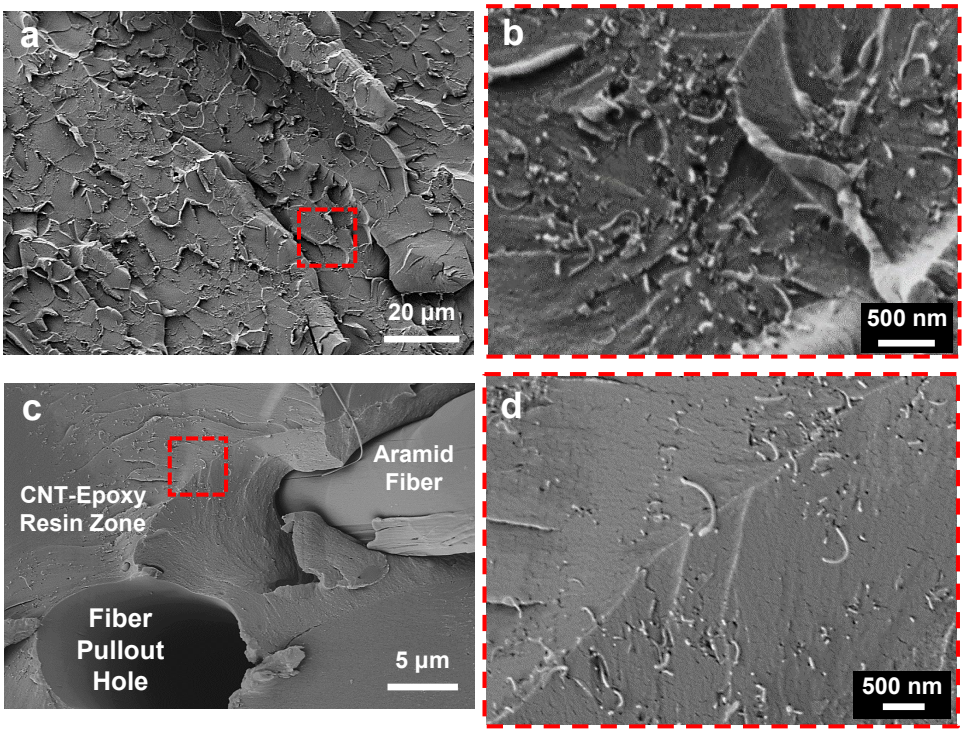

Figure 3. SEM images showing fracture surfaces of (a) the nanocomposite with 0.5 wt% CNTs and (b) a high magnification image in the dashed region of (a), and (c) the multiscale composite with aramid fibers and CNTs (0.5 wt%) dispersed in the matrix and (d) high magnification image of the dashed area in (c).

3.1.2 Composites with CNTs Localized at the Fiber Surfaces

In this study, different CNT coatings on fiber surfaces were produced using a dip-coating approach and EPD, which result in different thickness and density coatings on the fibers. Figures 4a-d and 4e-h show fracture surfaces of the composites with loosely (dip coating) and densely (EPD) concentrated CNTs, respectively. Figure 4a shows the fracture surface of the aramid composite with 0.75 wt% CNTs, where a non-uniform CNT-rich zone is observed bridging between adjacent fibers. As before, the aramid fibers are pulled-out of the matrix while the matrix in between the fibers shows a more brittle failure. The bridging of the CNT-rich region between fibers is also observed in the composites with 1.0 wt% CNTs (supplementary information, Fig. S3). Figure 4b shows the morphology of the epoxy-CNT-fiber interfacial region at a high magnification. The CNT coating appears to be fully infiltrated with the epoxy matrix but is locally inhomogeneous. Similar morphologies have been reported by Gao *et al*. [56] and Rausch and Mader [70] with dip coating techniques. Figure 4c shows the fracture surface of the E-glass composite with 1.0 wt% CNTs, where the fibers are fractured with small amounts of fiber pullout. The higher magnification image of the fiber surface, shown in Fig. 4d, reveals that CNTs remain on the surface of the glass fiber after fracture, suggesting stronger bonding between the CNT coating and the E-glass fiber surface than the aramid fibers. A matrix region where the fiber has debonded (supplementary information, Fig. S4) shows a similar level of texture.

In contrast with the dip-coating process, where CNTs are loosely concentrated around the fibers and are often observed bridging between fibers, the fracture surfaces of the composites produced using the EPD method show a more highly concentrated CNT coating that is confined near the fiber-matrix interface (Fig 4e). A higher magnification image of this region, shown in Fig. 4f, shows a uniform, dense coating that is confined within a few microns of the fiber surface. Figure 4g shows a side view where the fiber has debonded and the uniformity of the film along the length of the fiber is clear. In the EPD process, a highly porous film of the PEI-functionalized CNTs is formed on the fiber surfaces. The higher magnification images shown in Figs. 4f and 4h show that the epoxy resin has penetrated the porous network. It has been previously observed that the PEI-CNTs form a strong bond with the epoxy matrix due to the reaction between the amine functional groups in the ozone-PEI treated CNTs and epoxide groups in the resin [60,61].

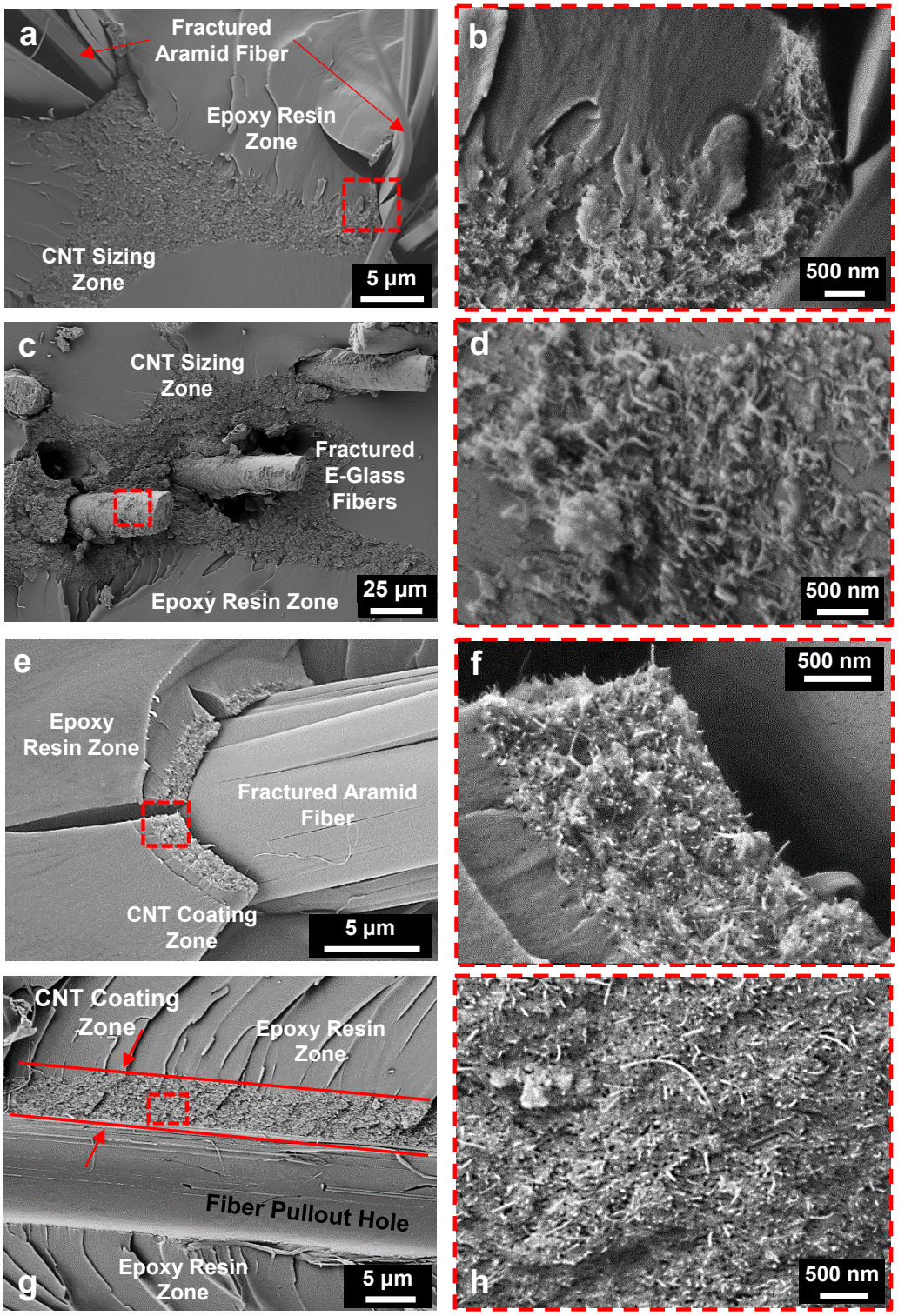

Figure 4. SEM images showing the fracture surfaces of the multiscale composites including (a) aramid-sizing (0.75 wt% CNT)/epoxy composite, (c) E-glass-sizing (1.0 wt% CNT)/epoxy composite, and aramid-EPD-CNT (1.8 wt%)/epoxy composite with (e) a cross-sectional view and (g) a longitudinal view; (b, d, f, h) the high magnification images of dashed regions in (a, c, e, g), respectively.

3.2 *Thermomechanical Response*

Figure 5 shows measurements of volumetric expansions as a function of temperature for nanocomposites and multi-scale composites with aramid and E-glass fibers. The CTE before the glass transition temperature (T_g) were measured from the linear portion of the curve beginning at ambient temperatures. Here, the T_g is taken as the onset of the abrupt change in slope in the linear thermal expansion curve. As shown in Fig. 5a, the neat epoxy shows a T_g near 121ºC and follows a crossover phase transition to its rubbery state after 130ºC in which the CTE becomes substantially higher than below T_g due to the increased segmental motion of polymer chains [71]. The sudden decrease in the thermal strain near T_g is likely due to the relieving of residual stresses. Post-curing results in an increase of crosslink density, the neat epoxy post-cured at 160ºC shows a 22% increased T_g. A sharp transition from glassy to rubbery is observed for the post-cured specimen because stresses are relieved during post cure and the specimen was cooled slowly. Compared with the neat epoxy, the nanocomposite with 0.25 wt% CNTs shows a 9% increase in CTE and 15% decrease in T_g while the 0.5 wt% CNT nanocomposite shows a slightly increased T_g and 8% reduction in CTE.

Figures 5b and 5c show the thermomechanical response of the fibrous composites. The aramid (Fig. 5b) and E-glass (Fig. 5c) composites without CNTs have a nearly identical T_g compared to the neat epoxy but a reduced CTE due to the confinement from the fibers. The thermal expansion of the nonwoven aramid and E-glass nonwoven fabric is also shown in Figs. 5b and 5c, respectively. The CNT sizing-based multiscale composite specimenss exhibit a slightly reduced T_g (~ -6%). In contrast, the multiscale composite with EPD-hybridized CNTs displays an unchanged T_g of 120ºC and about 9% reduction in CTE as compared to the plain composite. Table 4 summarizes the CTE and T_g measurements of the 12 different composites characterized in this study. Clearly, all composite systems expand as temperature raises until reaching glass transition. Later, the multiscale composites exhibited a reduced CTE as compared with the nanocomposites with an elevated CTE. For both sets of fibrous composites the CTE above T_g decreases and is dominated by expansion of the fiber because the Young's modulus of the matrix decreases substantially above glass transition. Also included in Table 4 is the T_g obtained from the TCR analysis, which is discussed in more detail in Section 3.4.

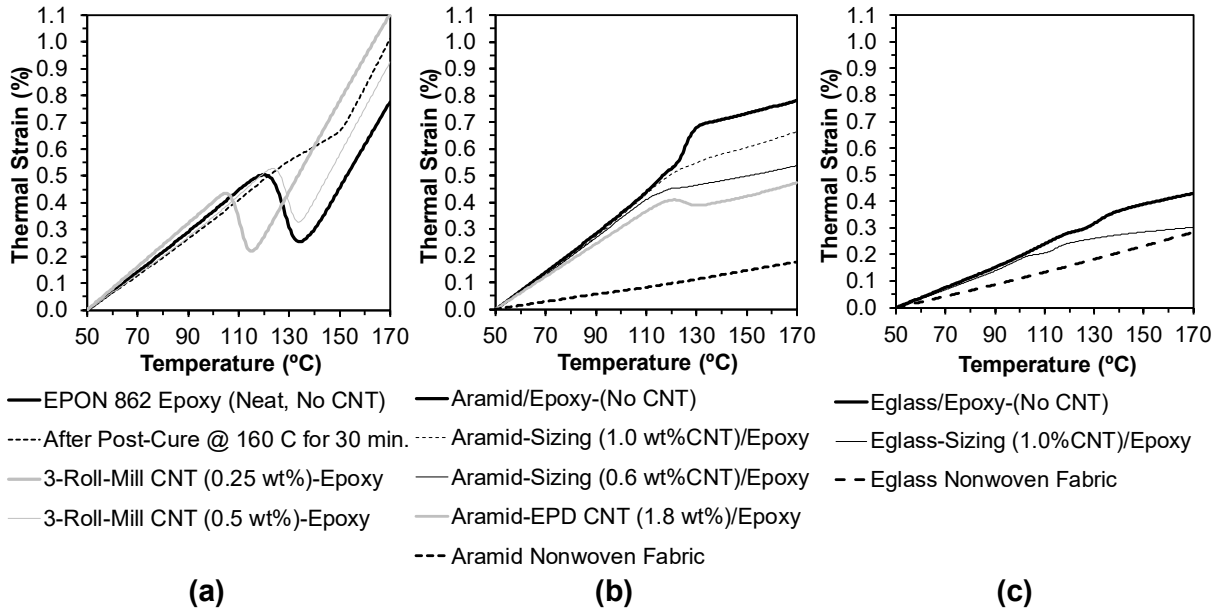

Figure 5. Thermomechanical responses showing dimensional changes as a function of temperature for (a) neat epoxy resin and CNT-based nanocomposites, (b) CNT-aramid, and (c) CNT-E-glass nonwoven multiscale composites produced via dip coating.

Table 4: Summary of CTE and T_g of a selected group of CNT-based composites measured using thermomechanical and thermoresistive methods.

Sample Group	CTE-10^{-6}/ºC ($T<T_g$)	T_g (ºC) from TMA[1]	T_g (ºC) from TCR Analysis[2]	Sample Group	CTE 10^{-6}/ºC ($T<T_g$)	T_g (ºC) from TMA[1]	T_g (ºC) from TCR Analysis[2]
Aramid nonwoven fabric (no CNT)	15±3	N/A	N/A[3]	Aramid/Epoxy	68±3	119±3	N/A
E-Glass nonwoven fabric (no CNT)	23±2			Aramid-Sizing (1.0%CNT)/Epoxy	65±4	114±5	114±3
EPON 862 Epoxy	74±4	121±3		Aramid-Sizing (0.6%CNT)/Epoxy	64±5	115±4	113±3
EPON 862 Epoxy (post-cured at 160ºC)	64±2	148±2		Aramid-EPD CNT (1.8%CNT)/Epoxy	61±3	120±3	119±2
3 roll mill CNT (0.25%)-Epoxy	81±3	105±3	104±2	E-Glass/Epoxy-	38±2	121±2	N/A
3 roll mill CNT (0.50%)-Epoxy	68±2	125±4	122±4	E-Glass-Sizing (1.0%CNT)/Epoxy	36±3	110±2	115±2

[1] All T_g values shown for TMA were taken as T_g^{onset} and are the average of four specimens; [2] TCR analysis is explained in Section 3.5; [3] Specimens without CNT are electrically insulating.

3.3 Thermal Stresses at the Fiber/Matrix Interface

Figures 6a and 6b show the development of residual stresses in the axial, hoop, and radial stresses that develop during cooling from a stress-free state at T_g (120ºC) to room temperature 25ºC), for the aramid/epoxy and E-glass/epoxy systems, respectively. As temperature decreases, these stresses increase linearly in the matrix of both composite systems, where $\sigma_{\theta\theta}$ and σ_{zz} are tensile and σ_{rr} is compressive. The axial stress, σ_{zz}, reaches about 18 MPa in both systems. Although aramid has a negative coefficient of thermal expansion, the much larger CTE of the polymer matrix results in a tensile axial stress in the matrix. However, σ_{rr} and $\sigma_{\theta\theta}$ are 17 MPa and -12 MPa, respectively in the E-glass/epoxy composite, which are about five times higher than those in the aramid/epoxy system. The aramid system has comparatively low stresses in the radial and hoop directions because the transverse CTE of the aramid is very similar to the epoxy. Compared with their ultimate strength of about 55 MPa as reported in our previous studies [6,71], these residual stresses are not negligible and may influence the thermoresistive behavior of the embedded CNT network.

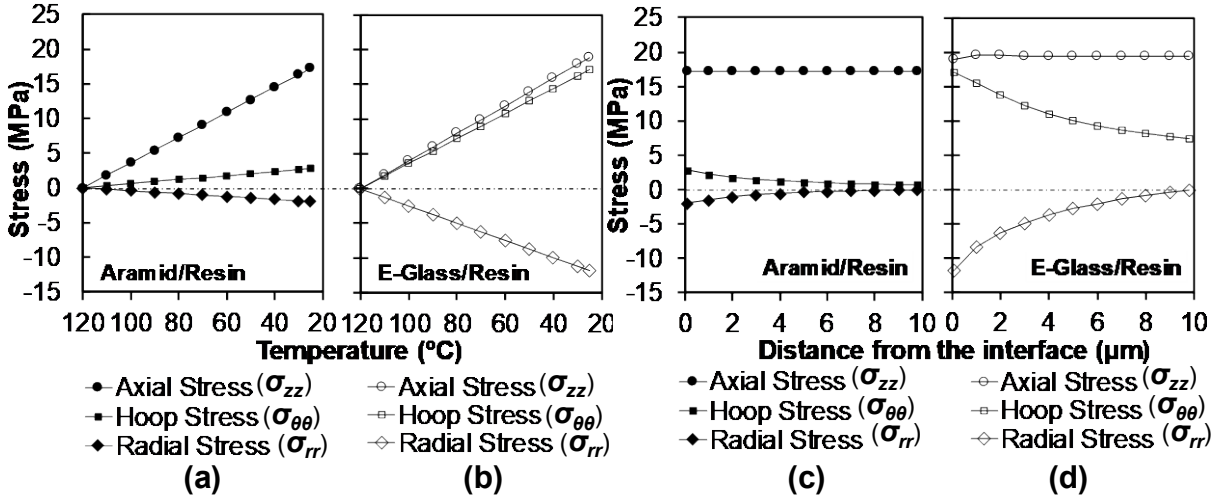

Figure 6. FEA results of (a, b) thermal residual stresses in the close vicinity of the fiber-resin interface in (a) aramid and (b) E-glass composite system as cooling from T_g to 25ºC, (c, d) residual stress distributions in the radial direction of the matrix from the fiber-resin interface in (c) aramid and (d) E-glass composite system at room temperature (25ºC).

Figures 6c and 6d show the stress distributions along the radial direction in the matrix with distance from the fiber/matrix interface at room temperature. The axial stress, σ_{zz}, is nearly the same for both composites. On the other hand, σ_{rr} and $\sigma_{\theta\theta}$ decrease with distance from the interface, exhibiting trends similar to those reported in the literature [62,63,66]. In the aramid/resin

composite, $\boldsymbol{\sigma_{rr}}$ and $\boldsymbol{\sigma_{\theta\theta}}$ in the are less than 1 MPa at a distance of 5 μm from the interface. Likewise, at the same location in the E-glass/resin composite $\boldsymbol{\sigma_{\theta\theta}}$ and $\boldsymbol{\sigma_{rr}}$ are 10 MPa and -2 MPa, respectively. For composites where CNTs are concentrated at the fiber/matrix interface, these residual stresses may have a significant influence on the thermoresistive behaviors.

3.4 *Thermoresistive Behaviors*

3.4.1 Nanocomposites and CNT/Fiber Composites with Randomly Dispersed CNTs

Figures 7a and 7c show the typical thermoresistive responses of the CNT-epoxy nanocomposite specimens with CNT concentrations of 0.25 wt% and 0.5 wt%, respectively. The left column of the figures shows the response under repeated cycling and the right column show the first heating cycle only. In general, both nanocomposites display a reversible trend with a PTC during thermal cycling between 25-145ºC. The nanocomposite with a lower CNT concentration of 0.25 wt% shows a larger thermoresistive response with a 13% resistance change over the temperature range as compared to a 5% change for the nanocomposite with 0.5 wt% CNTs. This thermoresistive sensitivity to CNT concentration is similar to the trend observed for piezoresistive mechanical/electrical coupling where the sensitivity to strain increases when concentrations get closer to the electrical percolation threshold [5]. The PTC is likely due to the thermal expansion of the epoxy matrix increasing the CNT-CNT electrical tunneling gap, leading to an increase in resistance [41]. As the temperature increases further, there is a more rapid increase in resistance, and as the polymer matrix reaches the T_g the matrix expands further due to the increased mobility of the polymer chains [52]. The curve of the nanocomposite with 0.25 wt% CNTs, shown in Fig. 7a, mirrors the overall thermal expansion from TMA. On the other hand, the nanocomposite with 0.5 wt% CNTs as shown in Fig. 7c, shows a PTC with a shape of the thermoresistive curve that is slightly concave-downward with a sharp increase above the T_g. With the increased content of CNTs, the reinforcement at the microscale may hinder the mobility of the polymer chains as the temperature approaches T_g, leading to a reduced rate of resistance growth [69,72,73].

The relationship of the temperature coefficient of resistance (TCR) has been widely used to evaluate the thermoresistive sensitivity of CNT nanocomposites [16,18,41,44,52]. The TCR responses of the nanocomposites during the first heating cycle are shown in Figs. 7b and 7d. In general, the TCR curves of the 0.25 wt% CNT nanocomposite shows more sharp changes with higher amplitudes than the nanocomposites with 0.5 wt% CNTs. At lower CNT concentrations it is likely that there are fewer redundant conductive pathways, leading to more pronounced TCR

changes with varying temperature, similar to the influence of CNT concentration on thermoresistive sensitivity. Similar TCR correlations have also been reported by others [16,41,43-45,49]. Structural changes of the CNT networks occur during glass transition, which causes the inflection points in thermoresistivity are seen as characteristic minima or maxima in the TCR curve. These are shown in Fig. 7b and 7d and are observed at 104ºC and 122ºC, respectively, which correlate well with the observed T_g based on the TMA results.

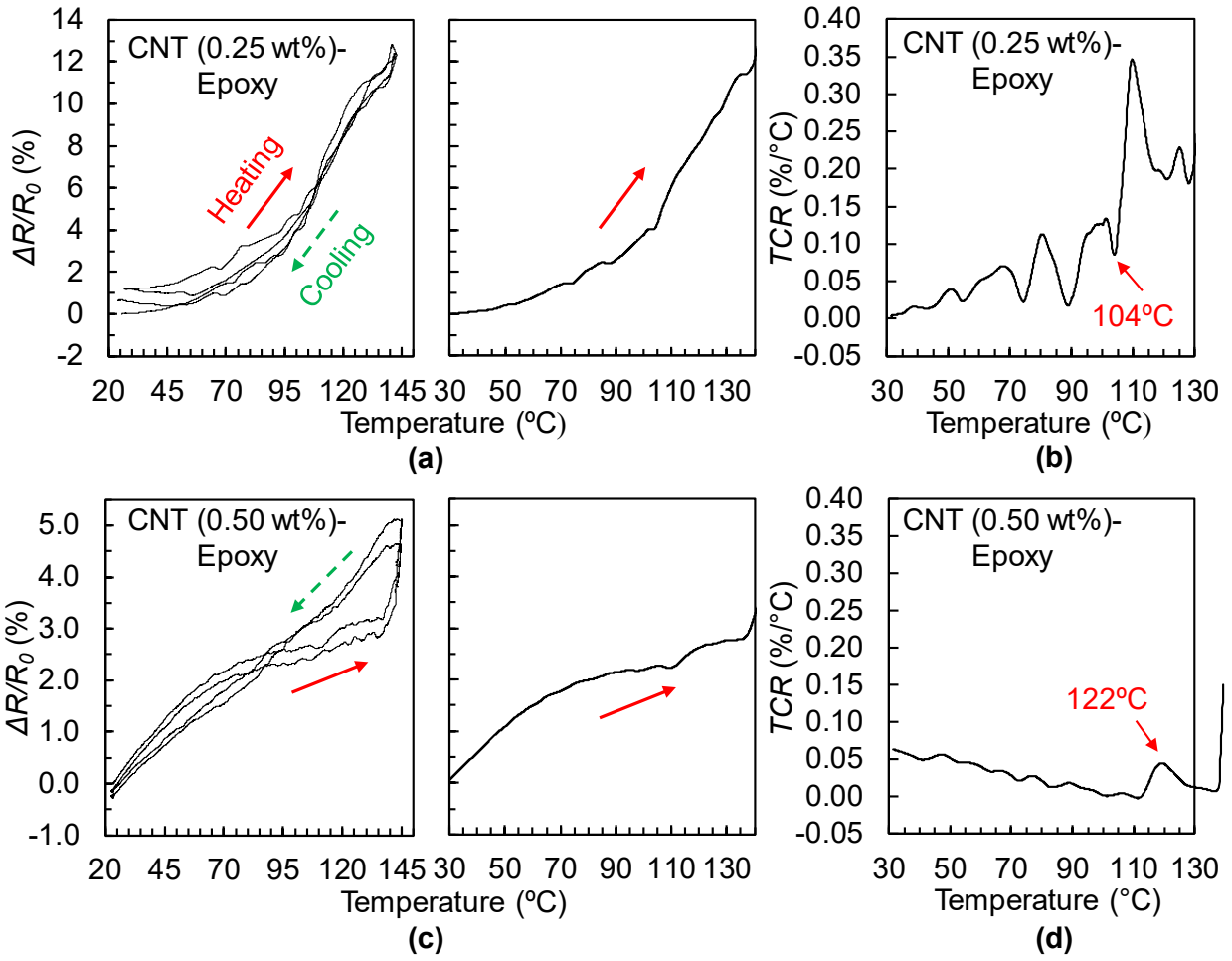

Figure 7. Thermoresistive responses of the CNT-epoxy nanocomposites under 25 to 145ºC thermal cycles. (a) Left, the resistance change response of nanocomposites with 0.25 wt% CNTs and, right, the first temperature ramp used to calculate the TCR, and (b) the TCR relationship for the first heating cycle; (c) Left, the resistance change response of nanocomposites with 0.5 wt% CNTs and, right, the first temperature ramp used to calculate the TCR, and (d) the TCR relationship for the first heating cycle.

Figures 8a and 8c show the thermoresistive responses of the aramid and E-glass fiber composites with 0.5 wt% CNTs dispersed in the epoxy matrix during 25-145ºC thermal cycles. Although both resistance change curves have very different shapes, they are reversible with minor cycle-to-cycle variations. These curves are distinctly different from the 0.5 wt% CNT nanocomposites, which always show PTC. At low temperatures both the aramid and E-glass fiber composites show NTC behavior. At higher temperatures, the aramid composite starts to show PTC behavior while the E-glass composite continues show NTC behavior. It is likely that the residual thermal stresses due to the mismatch in CTE between the matrix and fibers play a significant role in this different response. The fibers constrain the matrix during cooling, resulting in a residual tensile stress in the matrix. The aramid and E-glass composites with 0.5 wt% CNT dispersed in the matrix have a significantly different electrical resistivity of 38.0 Ω·m for aramid and 68.7 Ω·m for E-glass at room temperature (see Table 3), despite having similar fiber volume fractions. The difference in electrical resistivity for the aramid composite is 14% and the E-glass composite is 106% more than that of the 0.5 wt% CNT nanocomposite (33.4 Ω·m). In addition, the CTE below T_g of the aramid/epoxy composite is the same as the 0.5 wt% CNT while the CTE of the E-glass/epoxy is more than 40% less, suggesting that fiber constraint plays a significant role.

Figures 8b and 8d show the TCR relationships of the two multiscale composites with dispersed CNTs. The aramid composite (Fig. 8b) shows an increasing TCR, indicating that the thermoresistive sensitivity increases as thermal expansion dominates the thermoresistive response. The peak in the TCR curve is observed at 126ºC and correlates closely with the T_g measured by TMA. The TCR curve of the E-glass composite is shown in Fig. 8d and shows low amplitude variations with changing temperature and an average TCR of -300×10^{-6}/ºC. However, it is difficult to determine T_g based on the local features shown in Fig. 8d. For comparison, the thermoresistive responses of the aramid and E-glass multiscale composites with a CNT concentration of 0.25 wt% are included in supplementary information (Fig. S5). Both composites show an initial NPC response up to 65ºC and a sharp double-crossover transition in the region of 65-145ºC.

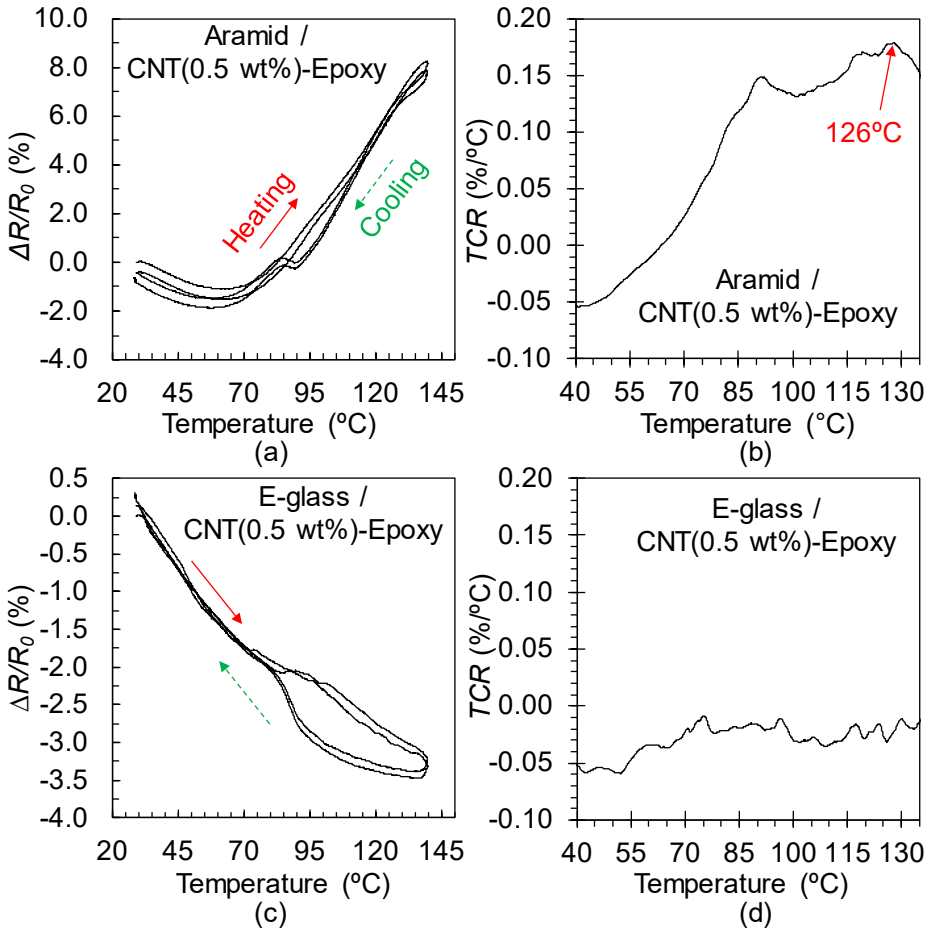

Figure 8. Thermoresistive responses of (a) aramid/dispersed CNT (0.5 wt%) epoxy and (c) E-glass/dispersed CNT (0.5 wt%) epoxy multiscale composites under 25 to 145ºC thermal cycles and (b, d) the corresponding TCR relationships for the initial heating cycle in (a and c).

3.4.2 Composites with Loosely Concentrated CNTs

The composites produced by dip-coating the fabric have a local structure of loosely concentrated CNTs around the fibers. The thermoresistive responses of composites with aramid fibers and different weight fractions of CNTs are shown in Figs. 9a-d. All composites show an overall NTC behavior with a double crossover transition in the heating ramp. Similar to the trends observed for the nanocomposites and the multiscale composites with dispersed CNTs, the composites with the higher CNT concentrations of 1 and 0.6 wt% (Figs. 9a and 9b) show less thermoresistive sensitivity than the composites with lower concentrations of 0.17 and 0.05 wt% (Figs. 9c and 9d). The thermoresistive response of all of these composites is significantly different from the nanocomposites and the aramid fiber composites with dispersed CNTs (Figs. 7 and 8).

The thermoresistive response of the composites produced by dip-coating can also be viewed in the context of the residual stresses in the composites. Here, the CNTs are more localized around the fibers and will be more influenced by the residual stresses that occur at the fiber-matrix interface. During heating, the residual thermal stresses in the multiscale composites release gradually and then the pre-tensioned CNT network likely contracts, reducing CNT tunneling gaps resulting in the observed NTC response up to 70ºC. Afterwards, the thermoresistive curves show a local increase of resistance that is likely influenced by the bulk thermal expansion of polymer matrix. The second crossover transition is observed at the local peak around 105ºC and decreases with increasing temperature. At temperatures higher than the T_g, the residual stresses are relieved.

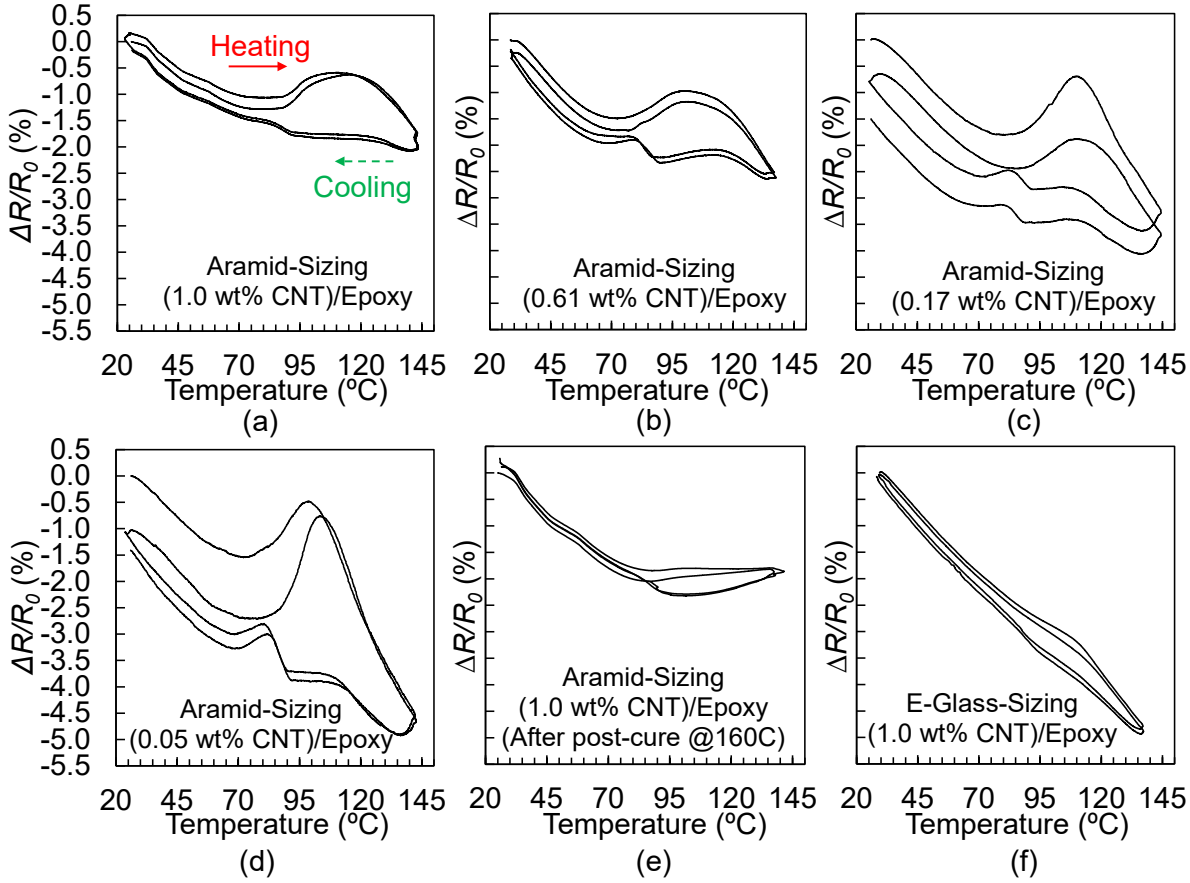

Figure 9. Thermoresistive responses of the aramid-sizing/epoxy multiscale composites with CNT loadings of (a) 1.0 wt%, (b) 0.61 wt%, (c) 0.17 wt%, and (d) 0.05% wt%, (e) the 1.0 wt% composite (a) after post-curing at 160°C for 30 minutes, and (f) E-glass-sizing (1.0 wt% CNT)/epoxy composite during 25-145°C thermal cycles (Note: $\Delta R/R_0$ in all Figs. are in [0.5%, -5.5%] scale).

All four different aramid composites (Figs. 9a-d) show some cycle-to-cycle resistance changes likely due to slight post-curing of the epoxy when the temperature is above T_g. Figure 9e shows the thermoresistive response of the composite with 1.0 wt% CNTs that was post-cured at 160ºC. The observed T_g for this composite of 148ºC (Table 4) is above the temperature range of the test, and there are minimal cycle-to-cycle variations. In addition, the peaks that occur in the heating cycle above 70ºC are eliminated, suggesting that the cross-link density of the matrix influences the thermoresistive response at higher temperatures.

For comparison, the thermoresistive behavior of the composite with E-glass fibers and 1.0 wt% CNTs (Fig. 9f) shows a continuous and decreasing NTC. There is a slight deviation from the linear response observed from 80-110ºC that corresponds to the temperature range where the peaks are observed in the aramid composites. As observed in the composites with dispersed CNTs, the constraint of the E-glass fibers likely dominates the overall response. As a reference, the bulk structure of CNT-coated E-glass fiber was replicated by depositing a CNT film on a planar glass substrate without introducing epoxy (supplementary information, Fig. S6a). The thermoresistive response (Fig. S6b) shows a linear NTC trend, further suggesting that the constraint of the fiber influences the overall thermoresistive response.

Figures 10a and 10b show the TCR responses of aramid-sizing/epoxy composites with 1.0 and 0.05 wt% CNTs, respectively. The TCR curve of the 0.05 wt%-CNT composite shows more dramatic fluctuations overall than the 1.0 wt%-CNT composite, indicating a more sensitive nanotube network with fewer CNTs that also correlates with the thermoresistive dependence of CNT concentration observed in the CNT-nanocomposites (Fig. 7). The post-cured 1.0 wt% composite shown in Fig. 10c at elevated temperature reveals a nearly constant TCR of 50×10^{-6}/ºC during 100-130ºC. Additionally, Fig. 10d shows the TCR curve of the E-glass-sizing/epoxy composite that reveals relatively low amplitude variation with a single transition. In Figs. 10b and 10d there are clear local minima at 118ºC, and 115ºC that correlateswell with the observed T_g measured by TMA. This is less evident in the 1.0 wt% CNT aramid composite, but the TCR curve does show a slight shoulder near the onset of glass transition around 114ºC.

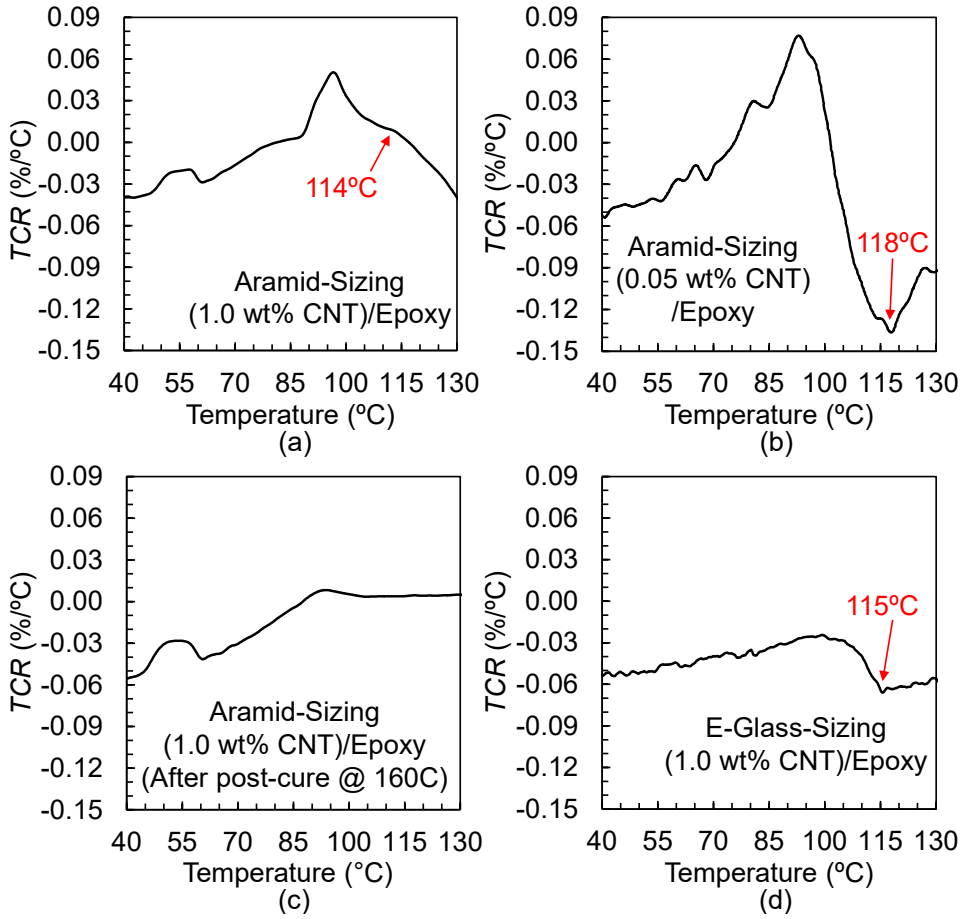

Figure 10. TCR relationships of the aramid-sizing/epoxy multiscale composites with CNT concentrations of (a) 1.0 wt% and (b) 0.05 wt%; (c) TCR relationship of the 1.0 wt% CNT aramid composite (shown in a) after post-curing at 160 °C for 30 minutes; (d) TCR relationship of the 1.0 wt% CNT E-glass/epoxy composite.

3.4.3 Composites with Densely Concentrated CNTs

It is clear that the residual stresses due to differential expansion of the fiber and matrix play a major role in the thermoresistive response. In order to shed more light on this behavior, the EPD approach was used to deposit a thin layer of functionalized CNTs on the fiber surfaces. Figures 11a and 11c show the typical thermoresistive responses of the aramid composites with different concentrations of CNTs. Both curves show an overall NTC response. The shapes of the curves are similar to the specimens produced using the dip-coating approach but show less pronounced nonlinear behavior at temperatures above 70ºC as compared to the dip-coated specimens (Fig. 9). The specimen with the lower concentration of CNTs, 1.8 wt% (Fig. 11c), shows a higher overall resistance change compared to the composite with higher CNT concentration, 3.4 wt% (Fig. 11a), following the inverse dependence of CNT concentration on thermoresistive sensitivity observed

previously. The magnitude of the resistance change over the temperature range of the test is several times higher than the resistance changes observed in the composites produced with the dip-coating approach. This further suggests that the stresses at the fiber-matrix interface play a significant role in the thermoresistive behavior. For the aramid composites the radial and hoop stresses are small (Fig. 6c), so the response is likely dominated by the stresses in the axial direction of the fiber because the CNTs are highly localized at the fiber-matrix interface.

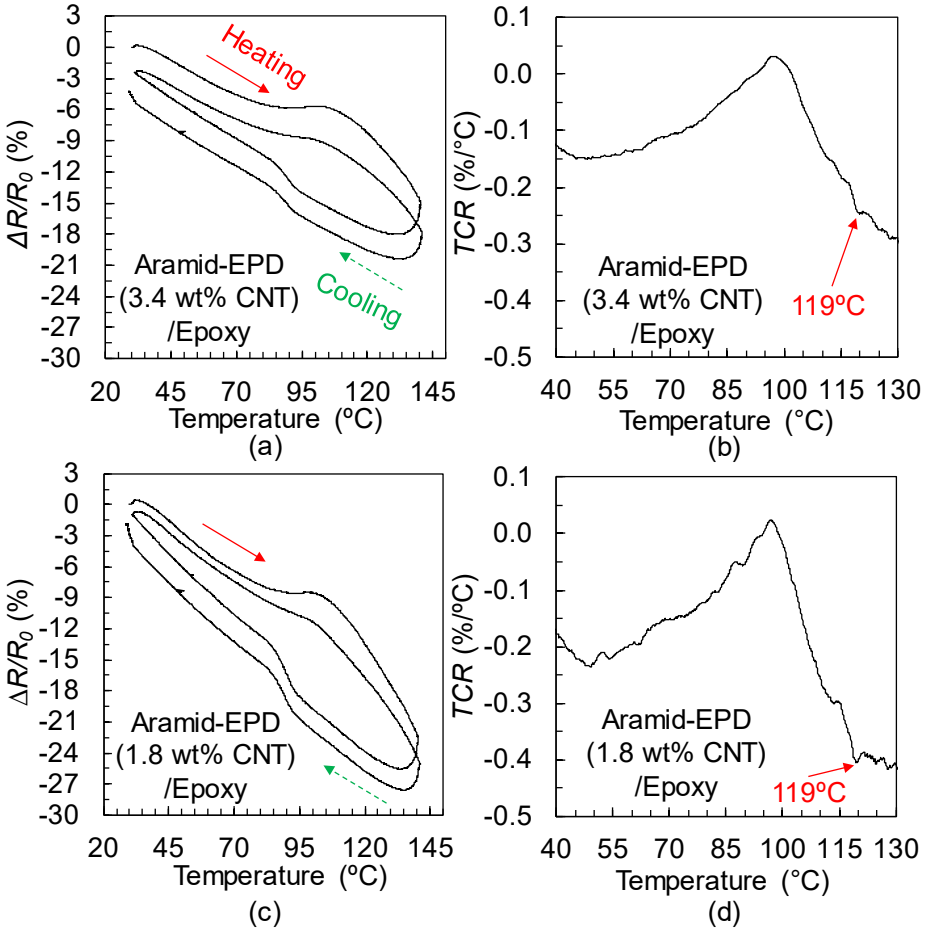

Figure 11. Thermoresistive responses of the aramid-CNT composites produced via EPD with CNT concentrations of (a) 3.4 wt% and (c) 1.8 wt%; (b, d) the corresponding TCR relationships for the 3.4 wt% and 1.8 wt% CNT composites in (a and c).

Similar to the CNT composites produced by dip-coating, the EPD processed composites also show some degree of cycle-to-cycle resistance changes, resulting from the slight post-curing of the epoxy matrix when heating above the T_g. Figures 11b and 11d show the corresponding TCR responses. The TCR curves are qualitatively similar to the TCR response for the dip-coated composites (Figs. 10a and 10b) where there is a peak occurring near 90-100ºC followed by a

decrease. For both of the TCR curves in Figs. 11b and 11d there is a local minimum that occurs at 119ºC after which the TCR curve begins to flatten. This temperature correlates closely with the measured onset of T_g by TMA.

4. Conclusions

CNT-based composites have found a number of applications as sensors, including mechanical strain/damage sensing, structural health monitoring, and process monitoring. The majority of these sensors have been studied in the laboratory under controlled temperature conditions. For applications these sensors will be exposed to varying temperatures during their use. As a result, it is important to understand the temperature-dependence of their electrical properties. We examined experimentally the thermoresistive behaviors of the CNT-based nanocomposites and multiscale composites containing CNTs and traditional fiber reinforcements. Composites were created with four different morphologies including (1) nanocomposite with randomly dispersed CNTs in epoxy, and multiscale CNT/fiber hybrid composites with (2) randomly dispersed CNTs in the matrix, (3) loosely-concentrated and (4) densely-concentrated CNTs near the fiber surface. The thermoresistive behavior was characterized for these composites over a temperature range of 25-145ºC. Combining the results from SEM, TMA and FE modeling with the *in situ* thermoresistive data of the CNT-based composites, we have found several key parameters that can directly influence the bulk thermoresistive responses including CNT concentration, CNT arrangement-and-rearrangement, fiber properties, interfacial interactions, thermal expansion, and polymer thermal transitions.

The two-phase CNT-epoxy nanocomposites show a PTC that is influenced primarily by volumetric expansion of the polymer matrix where expansion increases the CNT-CNT electrical tunneling gaps, leading to an increase in resistance. For all composites, the concentration of CNTs influences the thermoresistive sensitivity, where lower concentrations of CNTs have fewer redundant conductive pathways, which leads to more pronounced TCR changes with varying temperature. For these composites, it has also been shown that the TCR can be an indicator to detect glass transition temperatures, and the TCR response correlates closely with the onset of glass transition as measured by TMA. The multiscale composites demonstrated a reversible but crossover-shaped thermoresistive response suggesting that the thermoresistivity of these composites is influenced by structural changes of the CNT network and are affected by residual

thermal stresses and polymer thermal motions at different temperatures. The presence of fibers generates thermal residual stresses, leading to a pre-stressed CNT network upon cooling after manufacturing at elevated temperatures. These residual stresses develop on cooling from the stress-free state above the glass transition temperature. By adding fibers when CNTs are uniformly dispersed in the matrix the composites show an initial NTC response where the different types of fibers influence the response at higher temperatures. The room-temperature electrical resistivity for composites produced with aramid and E-glass fibers are significantly different and suggests that pre-tensioning of the polymer matrix on cooling is significant and depends on the fiber properties. Particularly, for composites with aramid fibers where CNTs are localized near the interface show double-crossover transitions at elevated temperatures. This behavior appears to be closely related to the crosslink density of the polymer matrix, since post-curing at higher temperatures minimizes the NTC to PTC transitions. Composites produced using the EPD approach have CNTs that are confined closely in the region of the fiber-matrix interface. These composites show the highest thermoresistive sensitivity which further highlights the influence of fiber-induced stresses on the thermoresistive response. The knowledge obtained from this study represents a first step in better understanding about the thermoresistive behavior of the CNT-based composites that can serve as a guide for developing CNT-based composite sensors for practical applications where these sensors are exposed to temperature variations.

Acknowledgements

This collaborative research has been supported by the US National Science Foundation Awards 1234830 and 1827729. We also thank Dr. Steve Sauerbrunn from Center for Composite Materials at the University of Delaware for his expertise in thermal analysis and helpful discussions.

References

[1] Li C, Thostenson ET, Chou T. Sensors and actuators based on carbon nanotubes and their composites: A review. Composites Sci Technol 2008;68(6):1227-1249.

[2] Thostenson ET, Ren Z, Chou T. Advances in the science and technology of carbon nanotubes and their composites: a review. Composites Sci Technol 2001;61(13):1899-1912.

[3] De Volder MF, Tawfick SH, Baughman RH, Hart AJ. Carbon nanotubes: present and future commercial applications. Science 2013;339(6119):535-539.

[4] Thostenson ET, Li C, Chou T. Nanocomposites in context. Composites Sci Technol 2005;65(3–4):491-516.

[5] Pandey G, Thostenson ET. Carbon nanotube-based multifunctional polymer nanocomposites. Polymer Reviews 2012;52(3):355-416.

[6] Dai H, Thostenson ET, Schumacher T. Processing and Characterization of a Novel Distributed Strain Sensor Using Carbon Nanotube-Based Nonwoven Composites. Sensors 2015;15(7):17728-17747.

[7] Gao L, Thostenson ET, Zhang Z, Chou T. Sensing of Damage Mechanisms in Fiber-Reinforced Composites under Cyclic Loading using Carbon Nanotubes. Advanced Functional Materials 2009;19(1):123-130.

[8] Zhang H, Liu Y, Kuwata M, Bilotti E, Peijs T. Improved fracture toughness and integrated damage sensing capability by spray coated CNTs on carbon fibre prepreg. Composites Part A: Applied Science and Manufacturing 2015;70:102-110.

[9] Dai H, Gallo GJ, Schumacher T, Thostenson ET. A Novel Methodology for Spatial Damage Detection and Imaging Using a Distributed Carbon Nanotube-Based Composite Sensor Combined with Electrical Impedance Tomography. J Nondestr Eval 2016;35(2):1-15.

[10] Zhang H, Bilotti E, Peijs T. The use of carbon nanotubes for damage sensing and structural health monitoring in laminated composites: a review. Nanocomposites 2015;1(4):167-184.

[11] Dai H, Thostenson ET. Large-Area Carbon Nanotube-Based Flexible Composites for Ultra-Wide Range Pressure Sensing and Spatial Pressure Mapping. ACS applied materials & interfaces 2019;11(51):48370-48380.

[12] Wang C, Xia K, Wang H, Liang X, Yin Z, Zhang Y. Advanced carbon for flexible and wearable electronics. Adv Mater 2019;31(9):1801072.

[13] Fan Q, Qin Z, Villmow T, Pionteck J, Pötschke P, Wu Y, Voit B, Zhu M. Vapor sensing properties of thermoplastic polyurethane multifilament covered with carbon nanotube networks. Sensors Actuators B: Chem 2011;156(1):63-70.

[14] Schroeder V, Savagatrup S, He M, Lin S, Swager TM. Carbon nanotube chemical sensors. Chem Rev 2018;119(1):599-663.

[15] Di Bartolomeo A, Sarno M, Giubileo F, Altavilla C, Iemmo L, Piano S, Bobba F, Longobardi M, Scarfato A, Sannino D. Multiwalled carbon nanotube films as small-sized temperature sensors. J Appl Phys 2009;105(6):064518.

[16] Matzeu G, Pucci A, Savi S, Romanelli M, Di Francesco F. A temperature sensor based on a MWCNT/SEBS nanocomposite. Sensors and Actuators A: Physical 2012;178:94-99.

[17] Yoo K, Lim L, Min N, Lee MJ, Lee CJ, Park C. Novel resistive-type humidity sensor based on multiwall carbon nanotube/polyimide composite films. Sensors Actuators B: Chem 2010;145(1):120-125.

[18] Aliev AE. Bolometric detector on the basis of single-wall carbon nanotube/polymer composite. Infrared Phys Technol 2008;51(6):541-545.

[19] Simmons TJ, Vera-Reveles G, González G, Gutiérrez-Hernández JM, Linhardt RJ, Navarro-Contreras H, González FJ. Bolometric properties of semiconducting and metallic single-walled carbon nanotube composite films. ACS Photonics 2015;2(3):334-340.

[20] Wei C, Dai L, Roy A, Tolle TB. Multifunctional chemical vapor sensors of aligned carbon nanotube and polymer composites. J Am Chem Soc 2006;128(5):1412-1413.

[21] Saito R, Fujita M, Dresselhaus G, Dresselhaus MS. Electronic structure of chiral graphene tubules. Appl Phys Lett 1992;60(18):2204-2206.

[22] Ebbesen T, Lezec H, Hiura H, Bennett J, Ghaemi H, Thio T. Electrical-conductivity of individual carbon nanotubes. Nature 1996;382(6586):54-56.

[23] Odom TW, Huang J, Kim P, Lieber CM. Structure and electronic properties of carbon nanotubes. The Journal of Physical Chemistry B 2000;104(13):2794-2809.

[24] Delaney P, Di Ventra M, Pantelides S. Quantized conductance of multiwalled carbon nanotubes. Appl Phys Lett 1999;75(24):3787-3789.

[25] Frank S, Poncharal P, Wang ZL, Heer WA. Carbon nanotube quantum resistors. Science 1998;280(5370):1744-1746.

[26] Skákalová V, Kaiser AB, Woo Y, Roth S. Electronic transport in carbon nanotubes: From individual nanotubes to thin and thick networks. Physical Review B 2006;74(8):085403.

[27] Bandaru PR. Electrical properties and applications of carbon nanotube structures. Journal of nanoscience and nanotechnology 2007;7(4-5):1239-1267.

[28] Fischer J, Dai H, Thess A, Lee R, Hanjani N, Dehaas D, Smalley R. Metallic resistivity in crystalline ropes of single-wall carbon nanotubes. Physical review B 1997;55(8):R4921.

[29] Lee R, Kim H, Fischer J, Lefebvre J, Radosavljević M, Hone J, Johnson A. Transport properties of a potassium-doped single-wall carbon nanotube rope. Physical Review B 2000;61(7):4526.

[30] Hone J, Llaguno M, Nemes N, Johnson A, Fischer J, Walters D, Casavant M, Schmidt J, Smalley R. Electrical and thermal transport properties of magnetically aligned single wall carbon nanotube films. Appl Phys Lett 2000;77(5):666-668.

[31] Bae DJ, Kim KS, Park YS, Suh EK, An KH, Moon J, Lim SC, Park SH, Jeong YH, Lee YH. Transport phenomena in an anisotropically aligned single-wall carbon nanotube film. Physical Review B 2001;64(23):233401.

[32] Rogers S, Kaiser A. Thermopower and resistivity of carbon nanotube networks and organic conducting polymers. Current Applied Physics 2004;4(2):407-410.

[33] Hu L, Hecht D, Grüner G. Percolation in transparent and conducting carbon nanotube networks. Nano Letters 2004;4(12):2513-2517.

[34] Cao C, Hu C, Xiong Y, Han X, Xi Y, Miao J. Temperature dependent piezoresistive effect of multi-walled carbon nanotube films. Diamond and Related materials 2007;16(2):388-392.

[35] Baumgartner G, Carrard M, Zuppiroli L, Bacsa W, de Heer WA, Forró L. Hall effect and magnetoresistance of carbon nanotube films. Physical Review B 1997;55(11):6704.

[36] Pöhls J, Johnson MB, White MA, Malik R, Ruff B, Jayasinghe C, Schulz MJ, Shanov V. Physical properties of carbon nanotube sheets drawn from nanotube arrays. Carbon 2012;50(11):4175-4183.

[37] Koratkar N, Modi A, Lass E, Ajayan P. Temperature effects on resistance of aligned multiwalled carbon nanotube films. Journal of nanoscience and nanotechnology 2004;4(7):744-748.

[38] Lu S, Chen D, Wang X, Xiong X, Ma K, Zhang L, Meng Q. Monitoring the manufacturing process of glass fiber reinforced composites with carbon nanotube buckypaper sensor. Polym Test 2016;52:79-84.

[39] Barberio M, Camarca M, Barone P, Bonanno A, Oliva A, Xu F. Electric resistivity of multi-walled carbon nanotubes at high temperatures. Surf Sci 2007;601(13):2814-2818.

[40] Barrau S, Demont P, Peigney A, Laurent C, Lacabanne C. DC and AC conductivity of carbon nanotubes-polyepoxy composites. Macromolecules 2003;36(14):5187-5194.

[41] Alamusi, Li Y, Hu N, Wu L, Yuan W, Peng X, Gu B, Chang C, Liu Y, Ning H, Li J. Temperature-dependent piezoresistivity in an MWCNT/epoxy nanocomposite temperature sensor with ultrahigh performance. Nanotechnology 2013;24(45):455501-455506.

[42] Cen-Puc M, Pool G, Oliva-Avilés A, May-Pat A, Avilés F. Experimental investigation of the thermoresistive response of multiwall carbon nanotube/polysulfone composites under heating-cooling cycles. Composites Sci Technol 2017;151:34-43.

[43] Njuguna MK, Galpaya D, Yan C, Colwell JM, Will G, Hu N, Yarlagadda P, Bell JM. Investigation on Temperature-Dependent Electrical Conductivity of Carbon Nanotube/Epoxy Composites for Sustainable Energy Applications. Journal of nanoscience and nanotechnology 2015;15(9):6957-6964.

[44] Zeng Y, Lu G, Wang H, Du J, Ying Z, Liu C. Positive temperature coefficient thermistors based on carbon nanotube/polymer composites. Sci Rep 2014;4:6684.

[45] Pang H, Chen Q, Bao Y, Yan D, Zhang Y, Chen J, Li Z. Temperature resistivity behaviour in carbon nanotube/ultrahigh molecular weight polyethylene composites with segregated and double percolated structure. Plastics, Rubber and Composites 2013;42(2):59-65.

[46] Gao J, Li Z, Peng S, Yan D. Temperature-resistivity behaviour of CNTs/UHMWPE composites with a two-dimensional conductive network. Polym Plast Technol Eng 2009;48(4):478-481.

[47] Cen-Puc M, Oliva-Avilés A, Avilés F. Thermoresistive mechanisms of carbon nanotube/polymer composites. Physica E: Low-dimensional Systems and Nanostructures 2018;95:41-50.

[48] Mohiuddin M, Hoa S. Temperature dependent electrical conductivity of CNT–PEEK composites. Composites Sci Technol 2011;72(1):21-27.

[49] Gau C, Kuo C, Ko H. Electron tunneling in carbon nanotube composites. Nanotechnology 2009;20(39):395705.

[50] Xiang Z, Chen T, Li Z, Bian X. Negative temperature coefficient of resistivity in lightweight conductive carbon nanotube/polymer composites. Macromolecular Materials and Engineering 2009;294(2):91-95.

[51] Balam A, Cen-Puc M, May-Pat A, Abot J, Avilés F. Influence of polymer matrix on the sensing capabilities of carbon nanotube polymeric thermistors. Smart Mater Struct 2019;29(1):015012.

[52] Lasater KL, Thostenson ET. In situ thermoresistive characterization of multifunctional composites of carbon nanotubes. Polymer 2012;53(23):5367-5374.

[53] Li Q, Xue Q, Gao X, Zheng Q. Temperature dependence of the electrical properties of the carbon nanotube/polymer composites. Express Polym Lett 2009;3(12):769-777.

[54] Xue W, Cui T. Characterization of layer-by-layer self-assembled carbon nanotube multilayer thin films. Nanotechnology 2007;18(14):145709.

[55] Loyola BR, Zhao Y, Loh KJ, La Saponara V. The electrical response of carbon nanotube-based thin film sensors subjected to mechanical and environmental effects. Smart Mater Struct 2012;22(2):025010.

[56] Gao S, Zhuang R, Zhang J, Liu J, Mäder E. Glass fibers with carbon nanotube networks as multifunctional sensors. Advanced Functional Materials 2010;20(12):1885-1893.

[57] Zhang J, Zhuang R, Liu J, Scheffler C, Mäder E, Heinrich G, Gao S. A single glass fiber with ultrathin layer of carbon nanotube networks beneficial to in-situ monitoring of polymer properties in composite interphases. Soft Materials 2014;12(sup1):S115-S120.

[58] Thostenson ET, Chou T. Processing-structure-multi-functional property relationship in carbon nanotube/epoxy composites. Carbon 2006;44(14):3022-3029.

[59] Dai H, Thostenson ET. Scalable and multifunctional carbon nanotube-based textile as distributed sensors for flow and cure monitoring. Carbon 2020;164:28-41.

[60] An Q, Rider AN, Thostenson ET. Electrophoretic deposition of carbon nanotubes onto carbon-fiber fabric for production of carbon/epoxy composites with improved mechanical properties. Carbon 2012;50(11):4130-4143.

[61] An Q, Rider AN, Thostenson ET. Hierarchical composite structures prepared by electrophoretic deposition of carbon nanotubes onto glass fibers. ACS applied materials & interfaces 2013;5(6):2022-2032.

[62] Shokrieh M, Daneshvar A, Akbari S. Reduction of thermal residual stresses of laminated polymer composites by addition of carbon nanotubes. Mater Des 2014;53:209-216.

[63] Shokrieh M, Safarabadi M. Three-dimensional analysis of micro-residual stresses in fibrous composites based on the energy method: a study including interphase effects. J Composite Mater 2012;46(6):727-735.

[64] Anagnostopoulos G, Parthenios J, Galiotis C. Thermal stress development in fibrous composites. Mater Lett 2008;62(3):341-345.

[65] Liao K, Tan Y. Influence of moisture-induced stress on in situ fiber strength degradation of unidirectional polymer composite. Composites Part B: Engineering 2001;32(4):365-370.

[66] Quek M. Analysis of residual stresses in a single fibre–matrix composite. Int J Adhes Adhes 2004;24(5):379-388.

[67] Detassis M, Pegoretti A, Migliaresi C, Wagner H. Experimental evaluation of residual stresses in single fibre composites by means of the fragmentation test. J Mater Sci 1996;31(9):2385-2392.

[68] Wisnom M, Gigliotti M, Ersoy N, Campbell M, Potter K. Mechanisms generating residual stresses and distortion during manufacture of polymer–matrix composite structures. Composites Part A: Applied Science and Manufacturing 2006;37(4):522-529.

[69] Montazeri A, Khavandi A, Javadpour J, Tcharkhtchi A. Viscoelastic properties of multi-walled carbon nanotube/epoxy composites using two different curing cycles. Mater Des 2010;31(7):3383-3388.

[70] Rausch J, Mäder E. Health monitoring in continuous glass fibre reinforced thermoplastics: Manufacturing and application of interphase sensors based on carbon nanotubes. Composites Sci Technol 2010;70(11):1589-1596.

[71] Dai H. An innovative sensing approach using carbon nanotube-based composites for structural health monitoring of concrete structures. PhD Dissertation, Univeristy of Delaware, United States 2017.

[72] Allaoui A, El Bounia N. How carbon nanotubes affect the cure kinetics and glass transition temperature of their epoxy composites?–a review. Express Polymer Letters 2009;3(9):588-594.

[73] Montazeri A. The effect of functionalization on the viscoelastic behavior of multi-wall carbon nanotube/epoxy composites. Mater Des 2013;45:510-517.